

Dynamics of Compression-Driven Gas-Liquid Displacement in a Capillary Tube

Callum Cuttle[✉] and Christopher W. MacMinn^{✉*}

Department of Engineering Science, University of Oxford, Oxford OX1 3PJ, United Kingdom

 (Received 23 December 2021; revised 20 October 2022; accepted 26 January 2023; published 13 March 2023)

We study two-phase displacement via the steady compression of an air reservoir connected to an oil-filled capillary tube. Our experiments and modeling reveal complex displacement dynamics depending on compression rate and reservoir volume that, for large reservoirs, depend on a single dimensionless compressibility number. We identify two distinct displacement regimes, separated by a critical value of the compressibility number. While the subcritical regime exhibits quasisteady displacement after an initial transient, the supercritical regime exhibits burstlike expulsion.

DOI: [10.1103/PhysRevLett.130.114001](https://doi.org/10.1103/PhysRevLett.130.114001)

The gas-driven displacement of viscous liquid from a confined geometry occurs in various natural and industrial systems, including subsurface storage of carbon dioxide [1,2], operation of fuel cells [3], reopening of airways [4,5], and displacement of subretinal blood during eye surgery [6]. Gas-liquid displacement is one of the simplest classes of two-phase flows because the viscosity of the gas is typically negligible, making these flows especially tractable to theoretical analysis and firmly establishing their role as the key model system in interfacial fluid dynamics [7]. Nonetheless, gas-driven displacements are inherently unsteady due to the interaction between compression of the gas and viscous resistance in the liquid. For example, recent work has identified nonmonotonic variations in pressure or invasion rates during displacement in porous media [3,8], episodic growth of intricate patterns during displacement of granular suspensions [9,10], and time-dependent growth of fractures during injection of foams into gels [11], despite the constant nominal injection rate in all cases. Here, we show that even the simplest gas-driven displacement is a complex dynamical system where springlike compression drives flow against a rate- and state-dependent resistance.

To elucidate the nonlinear dynamics underpinning these flows, we consider a model problem: displacement of viscous oil from a capillary tube by compressing a connected reservoir of air of initial volume V_i at a fixed nominal rate Q [Fig. 1(a)]. The fluid mechanics of this idealized system are fully captured by a simple model that reproduces our experimental observations both qualitatively and quantitatively, as discussed below. Yet, complex behavior emerges immediately from both experiments and theory: At the same Q , an experiment can either tend to a steady velocity after an initial transient when V_i is small [Fig. 1(b)(i)] or accelerate rapidly toward a burstlike expulsion when V_i is large [Fig. 1(b)(ii)]. Here, we show that these examples illustrate the two distinct displacement regimes that emerge from the coupling of springlike compression with viscous displacement. We show that this

problem is a specific realization of a simple dynamical system, the complex behavior of which can be captured with a reduced model comprising a nonlinear, first-order ordinary differential equation. This model reproduces and explains the contrasting dynamics shown in Fig. 1(b), as well as the sharp transition point between these two dynamical regimes.

Our experimental flow cell comprised a glass capillary tube of length 10 cm and inner radius $R = 0.66 \pm 0.01$ mm [Fig. 1(a)]. One end of the tube was connected to a sealed air reservoir of initial volume $V_i \in \{4, 8, 16, 32\} \pm 0.1$ mL; the other end fed into a bath of silicone oil at fixed hydrostatic pressure p_{HS} (viscosity $\mu = 0.096$ Pa s, surface tension $\gamma = 21$ mN m⁻¹, and density $\rho = 960$ kg m⁻³ at laboratory temperature $T_{\text{lab}} = 22 \pm 1$ °C; Dow Corning). Before each experiment, oil was drawn from the bath into the tube, filling an initial length $L = 56 \pm 1$ mm. Experiments were initiated by compressing the air reservoir at a fixed rate $Q \in \{0.05, 0.1, 0.2, 0.4, 0.8, 1.6\}$ mL/min, thus injecting air into the tube and expelling oil into the bath. We used imaging and image processing to measure the motion of the interface, the thickness of thin residual films deposited on the tube walls by the perfectly wetting oil, and the radius of curvature b of the air-oil interface. We also measured the gauge pressure p_g of the air relative to atmospheric pressure $p_{\text{atm}} = 101$ kPa, and thus calculated the viscous pressure drop $\Delta p = p_g - 2\gamma/b - p_{\text{HS}}$ across the oil slug (see Supplemental Material [12]).

For reference, we first consider an incompressible displacement at a rate Q (dashed lines in Fig. 2). Neglecting thin residual films, the air-oil interface must advance linearly with time t , such that its displacement relative to its initial position is $l = Qt/(\pi R^2)$ [Fig. 2(a)] and its velocity $u = dl/dt = Q/(\pi R^2)$ is constant [Fig. 2(b)]. The experiment ends at breakout time $t_{bo} = \pi R^2 L/Q$, when the interface reaches the outlet [i.e., $l(t_{bo}) = L$]. Assuming laminar Hagen-Poiseuille flow (see below), the pressure gradient in the oil $\Delta p/(L - l) = 8\mu Q/(\pi R^4)$ is

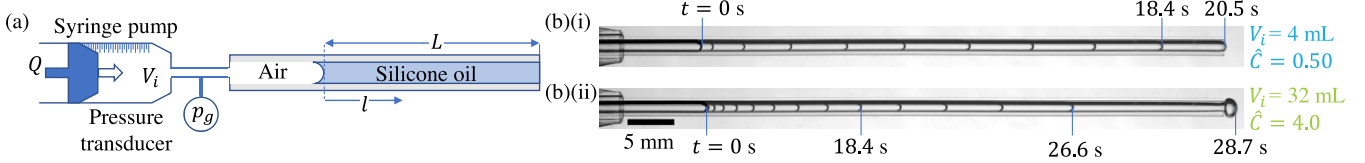


FIG. 1. Displacement of silicone oil from a capillary tube by the injection of air from a reservoir of initial volume V_i that is compressed at a constant volume rate Q using a syringe pump. (a) Experimental setup. We measure the displacement of the interface $l(t)$ relative to its initial position [$l(0) = 0$] as well as the gauge pressure p_g of the air. The oil slug has initial length L . (b) Experimental time lapses of overlaid frames at equal time steps $\Delta t = 2.05 \pm 0.02$ s show the motion of the interface; interframe spacing of interfaces is inversely proportional to interface velocity. (i) and (ii) are for $V_i = 4$ and 32 mL, respectively, and $Q = 0.2$ mL/min ($\hat{C} = 0.50$ and 4.0; see also Fig. 2).

constant and the pressure drop Δp decreases linearly from its maximum value of $8\mu QL/(\pi R^4)$ (reached instantaneously after flow starts at $t = 0$) to its breakout value of $\Delta p_{bo} = 0$ [Fig. 2(c)]. We normalize our compressible results below by these incompressible reference values, such that $\hat{l} = l/L$, $\hat{t} = t/(\pi R^2 L/Q)$, $\Delta \hat{p} = \Delta p/[8\mu QL/(\pi R^4)]$ and $\hat{u} = u/[Q/(\pi R^2)]$. Hatted quantities throughout are dimensionless.

In our experiments, the interface advances nonlinearly in time [Fig. 2(a)], initially moving slowly [$\hat{u} < 1$; Fig 2(b)] as the air compresses and pressurizes [$\Delta \hat{p}$ increases; Fig. 2(c)]. As oil drains and air pressure builds, \hat{u} increases. Once $\hat{u} > 1$, the oil flux exceeds the nominal flux imposed by the pump and the air begins decompressing [$\Delta \hat{p}$ decreases; Fig. 2(c)]. (Ref. [16] made similar observations, but across a more limited range of parameters.) As a result, the maximum in $\Delta \hat{p}$ occurs when $\Delta \hat{p}$ crosses the incompressible solution, for which $\Delta \hat{p} = 1 - \hat{l}$ and $\hat{u} = 1$. As V_i is increased (arrows in Fig. 2), we observe the transition from quasisteady to burstlike expulsion [e.g., Figs. 1(b)(i) and 1(b)(ii), respectively]. This transition is most apparent in the normalized velocities measured close to breakout [$\hat{u}(\hat{l} \approx 1)$], which increase dramatically from slightly above to more than 10 times the nominal velocity as V_i increases [not visible on the scale of Fig. 2(b); see Fig. 4(c)]. We next introduce a simple model that captures these observations.

We model the air as a fixed mass of isothermal ideal gas. We take the oil pressure at the outlet to be atmospheric, so the initial absolute air pressure is $p_{\text{atm}} + 2\gamma/R$. We neglect $p_{\text{HS}} \ll p_{\text{atm}}$ as it is arbitrary, but retain $2\gamma/R \ll p_{\text{atm}}$ for generality as it depends on the system parameters. The gauge pressure of the air is then

$$p_g(t) = (p_{\text{atm}} + 2\gamma/R) \frac{V_i}{V(t)} - p_{\text{atm}}, \quad (1)$$

where $V(t)$ is the current volume of air and $V(0) = V_i$. The syringe pump acts to decrease V at a steady rate Q , while the motion of the interface acts to increase V at a rate $\pi R^2(dl/dt)$; hence,

$$V(t) = V_i - Qt + \pi R^2 l(t). \quad (2)$$

We model the oil flow as Hagen-Poiseuille flow. In the absence of thin films, the interface velocity must be equal to the mean oil velocity, such that

$$\frac{dl}{dt} = \frac{R^2}{8\mu} \left(\frac{\Delta p}{L-l} \right), \quad (3)$$

where the viscous pressure drop along the oil slug is $\Delta p = p_g - 2\gamma/R$. Substituting Eqs. (1) and (2) into Eq. (3) and introducing \hat{l} , \hat{t} , and $\Delta \hat{p}$ from above yields

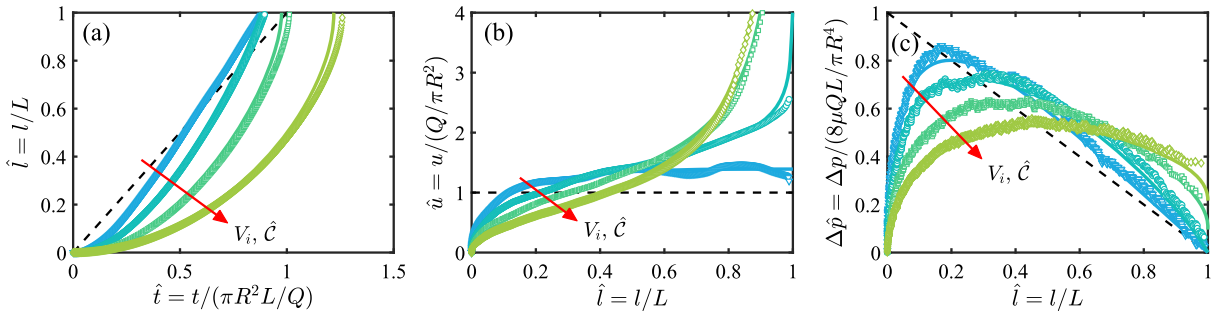


FIG. 2. (a)–(c) Experimental results (symbols) and numerical solutions to the full model with films (solid lines; see Supplemental Material [12]) for $Q = 0.2$ mL/min and $V_i = 4, 8, 16,$ and 32 mL ($\hat{C} = 0.50, 1.0, 2.0,$ and 4.0; dark to light). (a) Normalized displacement \hat{l} of the interface as a function of normalized time \hat{t} . (b)–(c) Normalized velocity \hat{u} and normalized pressure drop $\Delta \hat{p}$ as functions of \hat{l} . Dashed lines show corresponding incompressible behavior for reference. Arrows indicate increasing V_i and \hat{C} .

$$\frac{d\hat{l}}{d\hat{t}} = \left[\frac{\hat{p}_0 + 2/\hat{C}a}{\hat{V}_i + (\hat{l} - \hat{l})} \right] \left(\frac{\hat{l} - \hat{l}}{1 - \hat{l}} \right) = \frac{\Delta\hat{p}}{(1 - \hat{l})}. \quad (4)$$

Equation (4) is a nonlinear ordinary differential equation containing three independent nondimensional parameters: $\hat{p}_0 = \pi R^4 p_{\text{atm}} / (8\mu QL)$, comparing the compressive and viscous pressure scales; the capillary number $\hat{C}a = 8\mu QL / (\pi R^3 \gamma)$, comparing the viscous and capillary pressure scales; and $\hat{V}_i = V_i / (\pi R^2 L)$, comparing the initial volumes of air and oil.

To quantitatively compare with experiments requires the inclusion of thin films, which modify the interfacial capillary pressure and the kinematic relation between interface and oil velocities. We do so in the Supplemental Material [12] using well-established results and corrections. The full model with thin films (solid lines in Fig. 2) is in strong quantitative agreement with the experiments with no fitting parameters. As demonstrated below, however, the key qualitative features of this system can be captured with a much simpler model that does not include thin films.

Our model can be simplified by considering the limit of a much larger initial volume of air than of oil, $\hat{V}_i \gg 1$, which is the case in our experiments ($\hat{V}_i \approx 60\text{--}450$). In this limit, which corresponds to approximating the air as a linear spring, Eq. (4) reduces to

$$\frac{d\hat{l}}{d\hat{t}} \approx \left[\frac{\hat{p}_0 + 2/\hat{C}a}{\hat{V}_i} \right] \left(\frac{\hat{l} - \hat{l}}{1 - \hat{l}} \right) \equiv \frac{4}{\hat{C}} \left(\frac{\hat{l} - \hat{l}}{1 - \hat{l}} \right). \quad (5)$$

The system is then governed by a single nondimensional ‘‘compressibility number,’’

$$\hat{C} = \frac{32\mu Q V_i}{\pi^2 R^6 p_{\text{atm}}} \left(1 + \frac{2\gamma}{R p_{\text{atm}}} \right)^{-1}. \quad (6)$$

The reduced model, Eq. (5), captures most features of the full model and the experiments, and permits an implicit analytical solution given in the Supplemental Material [12]. The compressibility number \hat{C} can be interpreted by considering the characteristic rates at which compressive and viscous pressures vary, i.e., $\dot{P}_C = Q p_{\text{atm}} / V_i$ and $\dot{P}_V = 8\mu Q^2 / (\pi^2 R^6)$, respectively. Comparing with Eq. (6), we find that $\hat{C} \approx 4(\dot{P}_V / \dot{P}_C)$ when $2\gamma / (R p_{\text{atm}}) \ll 1$ (i.e., when the capillary pressure is much less than p_{atm}), as is the case for $R \gtrsim 10 \mu\text{m}$. Thus, \hat{C} measures the rate of viscous depressurization relative to compressive pressurization.

The effect of varying \hat{C} in the reduced model [Eq. (5)] is summarized in Fig. 3, which shows (normalized) breakout time \hat{t}_{bo} [Fig. 3(a)], breakout pressure drop $\Delta\hat{p}_{bo}$ [Fig. 3(b)], and breakout velocity \hat{u}_{bo} [Fig. 3(c)] as functions of \hat{C} . These breakout quantities all exhibit two distinct regimes separated by a critical compressibility number $\hat{C}_{\text{crit}} = 1$ (dashed lines). For all $\hat{C} \leq \hat{C}_{\text{crit}}$

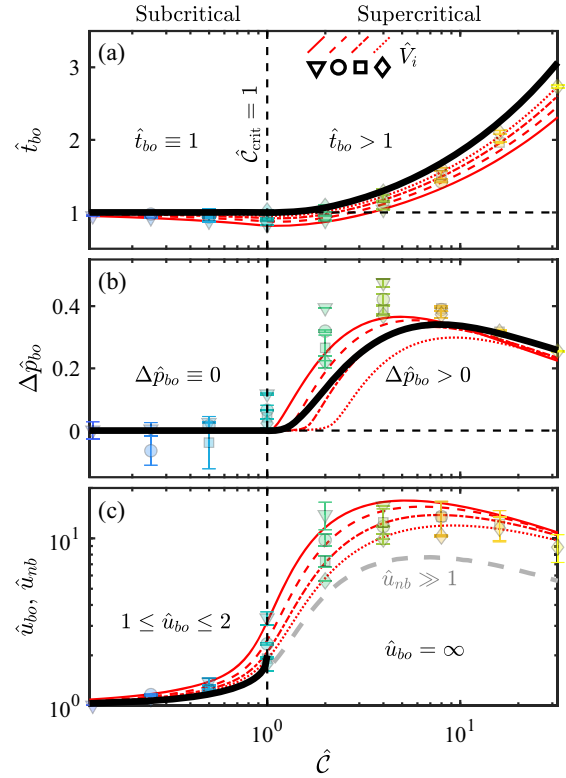


FIG. 3. Normalized breakout quantities calculated analytically from the reduced model [Eq. (5)]. Thick black curves show (a) \hat{t}_{bo} , (b) $\Delta\hat{p}_{bo}$, and (c) \hat{u}_{bo} as functions of \hat{C} . Vertical dashed lines at $\hat{C} = \hat{C}_{\text{crit}}$ separate the sub- and supercritical regimes. In (c), the near-breakout velocity \hat{u}_{nb} is plotted as a thick dashed curve. For comparison, \hat{t}_{bo} , $\Delta\hat{p}_{bo}$, and \hat{u}_{nb} are also shown for experiments (symbols) and the full model with thin films (red curves; see Supplemental Material [12]) for different \hat{V}_i [see legend in (a)].

(i.e., subcritical expulsion), breakout occurs at exactly $\hat{t}_{bo} \equiv 1$, meaning that the time taken to drain the oil is identical to that of an incompressible displacement at the same Q . As a result, the volume of air displaced by the piston at the moment of breakout is exactly equal to the volume of oil expelled, so the air returns precisely to its initial volume and pressure (i.e., $\Delta\hat{p}_{bo} \equiv 0$). For all $\hat{C} > \hat{C}_{\text{crit}}$ (i.e., supercritical expulsion), breakout is delayed [$\hat{t}_{bo} > 1$; Fig. 4(a)]. The volume displaced by the piston at the moment of breakout is greater than the volume of oil expelled, so the air is compressed and the system terminates with an overpressure, $\Delta\hat{p}_{bo} > 0$ [Fig. 4(b)]. These two scenarios have dramatically different consequences for the breakout velocity, $\hat{u}_{bo} = \lim_{\hat{l} \rightarrow 1} \Delta\hat{p} / (1 - \hat{l})$, which can only remain finite if $\Delta\hat{p}$ tends to zero at the same rate that \hat{l} tends to 1. This is the case only for subcritical expulsion, in which $1 \leq \hat{u}_{bo} \leq 2$. During supercritical expulsion, the overpressure at breakout results in infinite breakout velocities. Note that our use of the terms subcritical and supercritical refers only to the value of \hat{C}

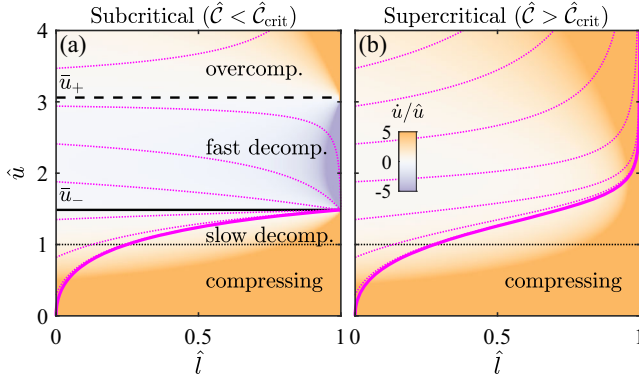


FIG. 4. Phase diagram in \hat{u} - \hat{l} space for (a) sub- and (b) supercritical expulsion dynamics ($\hat{C} = 0.88$ and 1.12 , respectively). Example trajectories with varying $\hat{u}(0)$ are plotted as magenta lines; the thick trajectory has $\hat{u}(0) = 0$, as in our experiments. Dashed, solid, and dotted black lines indicate \bar{u}_{\pm} and $\hat{u} = 1$, respectively. The color map indicates $\dot{\hat{u}}/\hat{u}$ (see color bar), which is saturated in regions close to $\hat{l} = 1$ and $\hat{u} = 0$.

relative to \hat{C}_{crit} , and is not intended to imply anything about the nature of the bifurcation. See Table S1 of the Supplemental Material [12] for analytical expressions for breakout quantities in each regime.

Measurements of breakout time \hat{t}_{bo} , breakout pressure $\Delta\hat{p}_{bo}$ and near-breakout velocity \hat{u}_{nb} are also plotted in Figs. 3(a)–3(c) for experiments and for the full model with films for different values of \hat{V}_i . We measure \hat{u}_{nb} two tube diameters from the outlet [$\hat{u}_{nb} = \hat{u}(\hat{l} = 1 - 4R/L)$] to reduce uncertainty by avoiding large \hat{u}_{bo} at high \hat{C} . Our experimental results clearly reflect a transition between sub- and supercritical regimes at $\hat{C} = \hat{C}_{\text{crit}}$, consistent with the predictions of the reduced model [Eq. (5)]. For $\hat{C} < \hat{C}_{\text{crit}}$, $\Delta\hat{p}_{bo} \approx 0$ to within experimental uncertainty [Fig. 3(b)], suggesting the pressure driving the flow vanishes at breakout, and the breakout velocities are modest [$\hat{u}_{nb} \gtrsim 1$; Fig. 3(c)]. For $\hat{C} > \hat{C}_{\text{crit}}$, we observe a marked rise in both $\Delta\hat{p}_{bo}$ and \hat{u}_{nb} , consistent with an overpressure driving burstlike expulsions with $\hat{u}_{nb} \sim 10$. The spread in the data and in the predictions of the full model for different $\hat{V}_i \propto V_i$ at fixed $\hat{C} \propto QV_i$ is due to residual films, the thickness of which depends strongly on $\hat{C}a \propto Q$.

The reduced model [Eq. (5)] describes a dynamical system in which the steady compression of a linear spring drives motion against a state-dependent viscous damper. To rationalize the emergence of such complex behavior from this simple, first-order dynamical system, we consider the generalized system in \hat{u} - \hat{l} phase space, as depicted in Fig. 4. Introducing the resistance $\hat{\omega} = 1 - \hat{l}$, Eq. (5) can be written as

$$\mathcal{R}(\hat{u}) = \mathcal{R}(\Delta\hat{p}) - \mathcal{R}(\hat{\omega}) = \frac{4}{\hat{\omega}\hat{C}} \left(\frac{1}{\hat{u}} - 1 + \frac{\hat{C}}{4}\hat{u} \right), \quad (7)$$

where $\mathcal{R}(\hat{x}) = \dot{\hat{x}}/\hat{x}$ is the relative rate of change of variable $\hat{x}(\hat{t})$, with $\dot{\hat{x}} = d\hat{x}/d\hat{t}$. Steady solutions \bar{u} of the reduced model are given by $\dot{\hat{u}}(\bar{u}) = 0$. There are two steady solutions for a subcritical expulsion,

$$\bar{u}_{\pm} = \frac{2}{\hat{C}} \left(1 \pm \sqrt{1 - \hat{C}} \right), \quad (8)$$

plotted as dashed and solid black lines in Fig. 4(a). These steady solutions merge and annihilate at a saddle-node bifurcation at $\hat{C} = \hat{C}_{\text{crit}}$, so that there are no real steady solutions for a supercritical expulsion. Physically, these steady displacements are states in which the driving pressure and the opposing resistance decrease at the same relative rate, $\mathcal{R}(\Delta\hat{p}) = \mathcal{R}(\hat{\omega})$.

For a subcritical expulsion [Fig 4(a)], the stability of each steady solution can be inferred from the sign of $\mathcal{R}(\hat{u})$ close to that solution, which is indicated by the color map in Fig. 4 (note $\hat{u} > 0$). Small perturbations decay close to \bar{u}_{-} and grow close to \bar{u}_{+} meaning that these solutions are, respectively, an attractor and a repeller. To understand the physical mechanisms that give each branch its stability, we consider how $\mathcal{R}(\Delta\hat{p})$ and $\mathcal{R}(\hat{\omega})$ vary with \hat{u} . When $\mathcal{R}(\Delta\hat{p}) > \mathcal{R}(\hat{\omega})$, the interface accelerates, $\mathcal{R}(\hat{u}) > 0$. This is the case in most of the phase diagram: when $\hat{u} < 1$ because the gas is compressing ($\Delta\hat{p} > 0$ and $\hat{\omega} < 0$), when $1 < \hat{u} < \bar{u}_{-}$ because the gas is decompressing slowly ($\Delta\hat{p} < 0$ and small), and when $\bar{u}_{+} < \hat{u}$ because the gas is overcompressed ($\Delta\hat{p}$ is large). When $\mathcal{R}(\Delta\hat{p}) < \mathcal{R}(\hat{\omega})$, however, the interface decelerates, $\mathcal{R}(\hat{u}) < 0$. This only occurs during subcritical expulsion when $\bar{u}_{-} < \hat{u} < \bar{u}_{+}$, for which the air undergoes fast decompression ($\Delta\hat{p} < 0$ and large). The fast decompression region thus gives rise to the two steady states \bar{u}_{\pm} and imparts their respective stabilities. In the supercritical phase space [Fig 4(b)], there are only two regions because the fast decompression region collapses and ceases to exist when the two steady states annihilate at $\hat{C} = \hat{C}_{\text{crit}}$. Hence, $\dot{\hat{u}} > 0$ for all \hat{u} .

Finally, the striking breakout features observed in our models and experiments are a consequence of the vanishing resistance at breakout. For subcritical expulsion, this means the attractive and repelling states become arbitrarily strong [$\mathcal{R}(\hat{u})$ diverges except at \bar{u}_{\pm}] and the system terminates at $\hat{u}_{bo} \equiv \bar{u}_{-}$. For supercritical expulsion, in the absence of steady solutions, \hat{u} diverges at the moment of breakout. To illustrate this, we plot several trajectories (magenta lines) in Figs. 4(a) and 4(b) for a range of initial velocities $\hat{u}(0)$. In our experiments, a nonzero $\hat{u}(0)$ could be imposed by pre-compressing the air before opening a valve to initiate flow. In the subcritical phase space [Fig. 4(a)], all trajectories with $\hat{u}(0) < \bar{u}_{+}$ terminate on the attractive solution \bar{u}_{-} , while those with $\hat{u}(0) > \bar{u}_{+}$ exhibit divergent \hat{u}_{bo} . In the supercritical phase space [Fig. 4(b)], \hat{u} diverges for all $\hat{u}(0)$.

In summary, we have shown that the gas-driven displacement of a confined viscous liquid is an example of a

simple, first-order dynamical system [Eq. (5)] that exhibits unexpectedly complex dynamical regimes. A single dimensionless parameter determines whether these dynamics are subcritical or supercritical, leading to “on-time” and quasisteady or delayed and burstlike dynamics, respectively. The key features of this idealized system are strikingly evident in our fluid-mechanical realization, demonstrating that the underlying dynamical framework can exert a powerful control on real-world systems. We therefore expect that analogous dynamics would occur in other nonlinear systems that couple the key ingredients embodied in the reduced model: a linear spring and a reducing, state-dependent resistance. In fluid mechanical systems, for instance, springlike compressibility can also originate from elastic walls, which act as volumetric capacitors [17]. More broadly, analogous time-dependent currents may occur in electrical circuits, which are an established test bed of nonlinear dynamics [18]; an idealized memristor-capacitor circuit has the right key ingredients and can therefore be represented by an equation that is analogous to the reduced model. In general, subcritical dynamics could be used to mitigate the presence of springlike components as a relatively minor and transient perturbation from corresponding “incompressible” behavior. Supercritical dynamics could wreak havoc if encountered unexpectedly (such as while squeezing a condiment bottle), but could also be exploited as a new design tool—for example, as a means of detecting otherwise-imperceptible flows or currents via passive amplification.

We are grateful to Clive Baker for technical support. We thank Dominic Vella and Anne Juel for helpful discussions. This work was supported by the European Research Council (ERC) under the European Union’s Horizon 2020 Programme (Grant No. 805469) and by the John Fell OUP Research Fund (Grant No. 132/012).

*christopher.macminn@eng.ox.ac.uk

- [1] S. Berg and H. Ott, Stability of CO₂-brine immiscible displacement, *Int. J. Greenhouse Gas Contr.* **11**, 188 (2012).
- [2] B. Zhao, C. W. MacMinn, and R. Juanes, Wettability control on multiphase flow in patterned microfluidics, *Proc. Natl. Acad. Sci. U.S.A.* **113**, 10251 (2016).
- [3] C. H. Lee, B. Zhao, R. Abouatallah, R. Wang, and A. Bazylak, Compressible-gas invasion into liquid-saturated porous media: Application to polymer-electrolyte-membrane electrolyzers, *Phys. Rev. Appl.* **11**, 054029 (2019).
- [4] A. L. Hazel and M. Heil, Three-dimensional airway reopening: the steady propagation of a semi-infinite bubble into a buckled elastic tube, *J. Fluid Mech.* **478**, 47 (2003).
- [5] L. Ducloué, A. L. Hazel, A. B. Thompson, and A. Juel, Reopening modes of a collapsed elasto-rigid channel, *J. Fluid Mech.* **819**, 121 (2017).
- [6] G. Pappas, N. Vidakis, M. Petousis, V. Kounali, and A. Korlos, An innovatory surgical technique for submacular hemorrhage displacement by means of a bioengineering perspective, *Vision* **5**, 23 (2021).
- [7] J. Casademunt, Viscous fingering as a paradigm of interfacial pattern formation: Recent results and new challenges, *Chaos* **14**, 809 (2004).
- [8] C. Louriou, H. Ouerfelli, M. Prat, M. Najjari, and S. B. Nasrallah, Gas injection in a liquid saturated porous medium. Influence of gas pressurization and liquid films, *Transp. Porous Media* **91**, 153 (2011).
- [9] B. Sandnes, E. G. Flekkøy, H. A. Knudsen, K. J. Måløy, and H. See, Patterns and flow in frictional fluid dynamics, *Nat. Commun.* **2**, 288 (2011).
- [10] B. Sandnes, E. G. Flekkøy, and K. J. Måløy, Stick slip displacement of confined granular mixtures: Bubble expansion, *Eur. Phys. J. Spec. Top.* **204**, 19 (2012).
- [11] C.-Y. Lai, B. Rallabandi, A. Perazzo, Z. Zheng, S. E. Smiddy, and H. A. Stone, Foam-driven fracture, *Proc. Natl. Acad. Sci. U.S.A.* **115**, 8082 (2018).
- [12] See Supplemental Material at <http://link.aps.org/supplemental/10.1103/PhysRevLett.130.114001> for more information on the experimental methods, data analysis, and mathematical modeling, and which includes Refs. [13–15].
- [13] P. Aussillous and D. Quéré, Quick deposition of a fluid on the wall of a tube, *Phys. Fluids* **12**, 2367 (2000).
- [14] F. P. Bretherton, The motion of long bubbles in tubes, *J. Fluid Mech.* **10**, 166 (1961).
- [15] E. Klaseboer, R. Gupta, and R. Manica, An extended Bretherton model for long Taylor bubbles at moderate capillary numbers, *Phys. Fluids* **26**, 032107 (2014).
- [16] F. Khemili, I. Bahrini, and M. Najjari, Oil drainage in a capillary tube: Experimental and numerical study, *Microgravity Sci. Technol.* **33**, 33 (2021).
- [17] G. Guyard, F. Restagno, and J. D. McGraw, Elastohydrodynamic relaxation of soft and deformable microchannels, *Phys. Rev. Lett.* **129**, 204501 (2022).
- [18] J. J. Healey, D. S. Broomhead, K. A. Cliffe, R. Jones, and T. Mullin, The origins of chaos in a modified Van der Pol oscillator, *Physica (Amsterdam)* **48D**, 322 (1991).